Journal of Marine Research, 51, 497–513, 1993

Model of frontogenesis: Subduction and upwelling

by Dong-Ping Wang[1]

ABSTRACT

A high-resolution, three-dimensional, primitive-equation model is used to study frontogenesis. The initial state includes a surface front and geostrophic jet. A small initial disturbance grows rapidly into a steepened backward-breaking wave, characterized by narrow wave trough and broad wave crest. Analysis of the energetics indicates that the unstable waves are generated by baroclinic instability. The wavelength scales as the baroclinic deformation radius, but the growth rate appears to be much faster than found in previous primitive-equation model studies. The predicted downward velocity also is an order of magnitude greater than found in previous model studies.

As the amplitude of unstable wave becomes very large, a narrow density front whose width is less than the deformation radius, is formed in the wave trough. The frontal zone is marked by high cyclonic vorticity (relative vorticity $> f$) and intense surface subduction (50–100 m day^{-1}). The frontogenesis is caused by the interaction between synoptic-scale confluence and mesoscale convergence. The strong vertical circulation associated with frontal waves may play a major role in the material exchange and biological production in frontal zone.

1. Introduction

Surface frontal features with length scales of 10–100 km are commonly found along the shoreward edge of the Gulf Stream. These frontal features typically are marked by a series of backward-breaking waves (shingles). The vertical structures of frontal waves were described, for example, by Bane *et al.* (1981) and Lee and Atkinson (1983) from observations in the South Atlantic Bight. The frontal waves were characterized by a shallow filament of warm water trailing behind the wave crest and a deep cyclonic eddy encircling the wave trough. The wavelength was about 180 km, corresponding to $2\pi L_d$ (L_d = deformation radius). Chew *et al.* (1985) found upwelling in the wave crest and subduction in the wave trough. They estimated from the displacement of isotherms a vertical velocity of about 50–100 m day^{-1}. Osgood *et al.* (1987) obtained similar results from the analysis of heat budget; moreover, they found that during frontal waves, subduction was much stronger than upwelling. The intense surface subduction contributed to the deep chlorophyll maximum layer (Yoder, 1985) and also led to traces of subsurface anomaly (Lillibridge *et al.,* 1990).

1. Marine Sciences Research Center, State University of New York, Stony Brook, New York, 11794-5000, U.S.A.

Dewey *et al.* (1991) mapped velocity and density structures across a large cold filament (frontal wave) off central California. The filament was characterized by a sloping density front about 200 m deep with density contrast of 2 σ_t (their Fig. 5); the corresponding deformation radius is 20 km. Estimate of the wavelength is very subjective. Nevertheless, the separation distance between two cold tongues (their Fig. 1) was about 120 km ($2\pi L_d$). The observations also indicated that the horizontal shears were much stronger on the cyclonic (cold) side than on the anticyclonic side. Also, the warm, fresh surface water on the northern (anticylconic) side of the filament was clearly separated from the cold, more saline surface water (the inshore water) on the southern (cyclonic) side (also see Strub *et al.,* 1991). This suggested that the cold inshore water was drawn down on the cyclonic side of the jet (Kadko *et al.,* 1991). Swenson *et al.* (1992) computed the vertical velocity from the time rate of change of the relative vorticity following a cluster of drifters. They obtained a maximum downward velocity of 60 m day^{-1}.

Garvine *et al.* (1988) mapped shelf-slope frontal waves off the New England coast. They found protruding shelf water filaments that curled backward to encircle a cyclonic eddy. The wavelength also was about $2\pi L_d$. The subducted water often appeared as detached parcels of cold anomaly. Wang *et al.* (1988) found similar frontal features off the northeast Spanish coast. The subducted surface water formed a layer of low-salinity anomaly at the base of the front. They obtained a maximum downward velocity of about 100 m day^{-1} from the rate of convergence of surface drifters. The frontal waves also are common in the open ocean (Subtropical Front). Pollard and Regier (1992) derived a maximum vertical velocity of 40 m day^{-1} using the omega equation analysis; similar results were obtained by Rudnick and Weller (1993) from the analysis of heat budget.

The frontal waves most likely are generated by the flow instabilities. While the basic mechanism of linear stability of a baroclinic current is fairly well understood (Pedlosky, 1979), no previous ocean circulation model study has been able to predict the strong surface subduction of 50–100 m day^{-1}. In this study, we demonstrate how the intense vertical circulation can arise from frontogenesis in baroclinic waves. Our objective is to construct a theoretical basis that can be used for analysis of the cross-frontal material exchange.

2. Numerical model

a. Governing Equations. The formulation of a time-dependent, three-dimensional, primitive-equation, general ocean circulation model was described in Wang (1989). The equations of motion, the hydrostatic equation, the continuity equation, and the conservation equation are,

$$\frac{Du}{Dt} - fv = -\frac{\partial P}{\partial x} + \frac{\partial}{\partial z}\left(A_v\left(\frac{\partial u}{\partial z}\right)\right) + A_h\nabla^2 u \tag{1}$$

$$\frac{Dv}{Dt} + fu = -\frac{\partial P}{\partial y} + \frac{\partial}{\partial z}\left(A_v\left(\frac{\partial v}{\partial z}\right)\right) + A_h\nabla^2 v \tag{2}$$

$$0 = \frac{\partial u}{\partial x} + \frac{\partial v}{\partial y} + \frac{\partial w}{\partial z} \tag{3}$$

$$0 = -\frac{\partial P}{\partial z} + \rho g \tag{4}$$

$$\frac{DT}{Dt} = \frac{\partial}{\partial z}\left(K_v\left(\frac{\partial T}{\partial z}\right)\right) + K_h\nabla^2 T \tag{5}$$

where $D/Dt = \partial/\partial t + u\partial/\partial x + v\partial/\partial y + w\partial/\partial z$, u, v, and w are cross-channel, along-channel, and vertical velocities, ρ is density, f is constant Coriolis parameter ($f = 10^{-4}\text{s}^{-1}$), P is pressure, T is equivalent temperature which is assumed to vary linearly with density, A_v is vertical eddy viscosity, A_h is horizontal eddy viscosity, K_v is vertical eddy diffusivity and K_h is horizontal eddy diffusivity. The vertical eddy coefficients are determined from Munk-Anderson formula (Munk and Anderson, 1948) with neutral values = 10^2 cm^2 s^{-1} and 1 cm^2 s^{-1} for eddy viscosity and eddy diffusivity. Actual vertical eddy coefficients are small in stratified regions. In the base case, the horizontal eddy coefficient = 10^5 cm^2 s^{-1}.

b. Formulation. In ocean general circulation models, all finite-difference operators ideally should have second-order (centered-difference) accuracy. However, in the transport equation (Eq. 5), use of centered-difference scheme may create spurious (negative) mass near a sharp gradient, which could cause severe numerical error (Kielmann and Kase, 1987). The upwind scheme will overcome this problem, but it only has first-order accuracy (too much artificial smoothing). To resolve this difficulty, a flux corrected transport (FCT) scheme which is almost second-order (Smolarkiewicz, 1983), is used in our model. We should caution that the numerical problem in dealing with a narrow frontal zone is difficult.

The model domain is a periodic channel, 60 km long, 80 km wide and 200 m deep. In a periodic channel setting, the channel length corresponds to one (or multiple) wavelength. At the wall, the normal velocity is set to zero (a slip boundary). At the surface, there is no wind stress. At the bottom, the friction is described by a quadratic law with drag coefficient = 3×10^{-3}. The horizontal resolution is 2 km, the vertical resolution is 20 m and the internal time step is 400 s.

The initial condition is a two-dimensional density front. In the base case the initial density is:

$$\rho = 26.2 - 0.5\left(1 - \tanh\left(\frac{x}{4}\right)\right)\exp\left(-\frac{z}{80}\right) \tag{6}$$

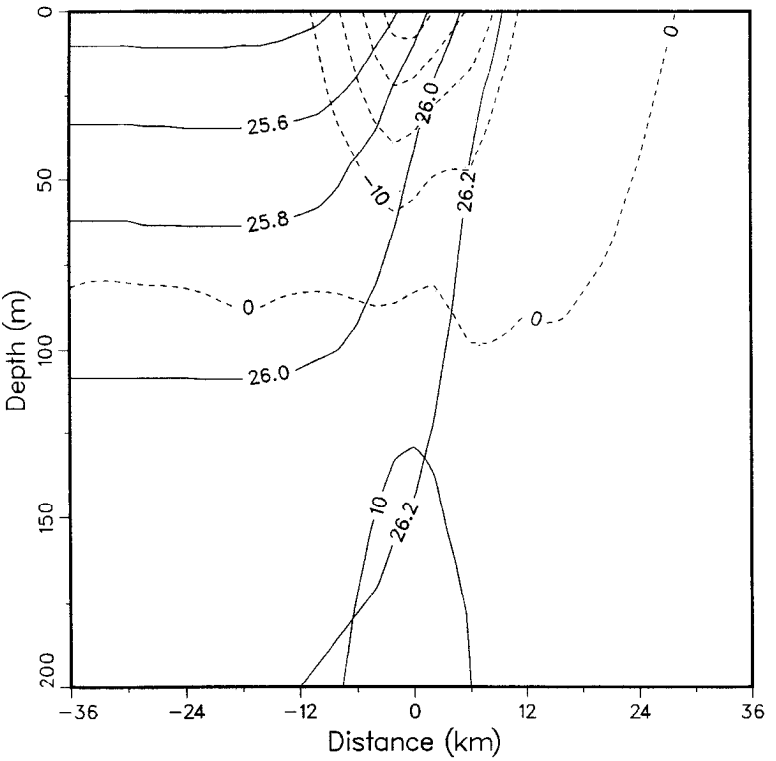

Figure 1. Initial density (solid lines) and velocity (dashed lines) distribution.

where ρ is in σ_t, x is in km ($x = 0$ is the center of channel) and z is in m ($z = 0$ is the free surface). The initial velocity structure is geostrophic; the arbitrary constant (reference velocity) is determined by setting the total transport equal to zero. Figure 1 shows the initial velocity and density distribution. The surface jet is about 20 km wide and 100 m deep, and has maximum speed $U = 45$ cm s^{-1}. To compare with an ideal two-layered system, the initial state can be approximated by density contrast $\Delta\rho = 1$ σ_t and layer depth $H = 100$ m. The internal gravity wave speed c_o, $(g\Delta\rho H)^{1/2}$, is 100 cm s^{-1}, the baroclinic deformation radius L_d, $c_o f^{-1}$, is 10 km. Thus, the jet width is $2L_d$, the maximum jet speed is $0.5c_o$ and the Rossby number R_o, $U(fL_d)^{-1}$, is 0.4.

3. Frontogenesis

a. Base case. For the periodic boundary condition, it is necessary to choose an appropriate wavelength. According to quasi-geostrophic theory, the most unstable baroclinic wave scales as the deformation radius, that is, the wavelength $= 2\pi L_d$ (Pedlosky, 1979). For $L_d = 10$ km, we chose the channel length equal to 60 km. Initially, the mean frontal position is perturbed by a small disturbance of amplitude

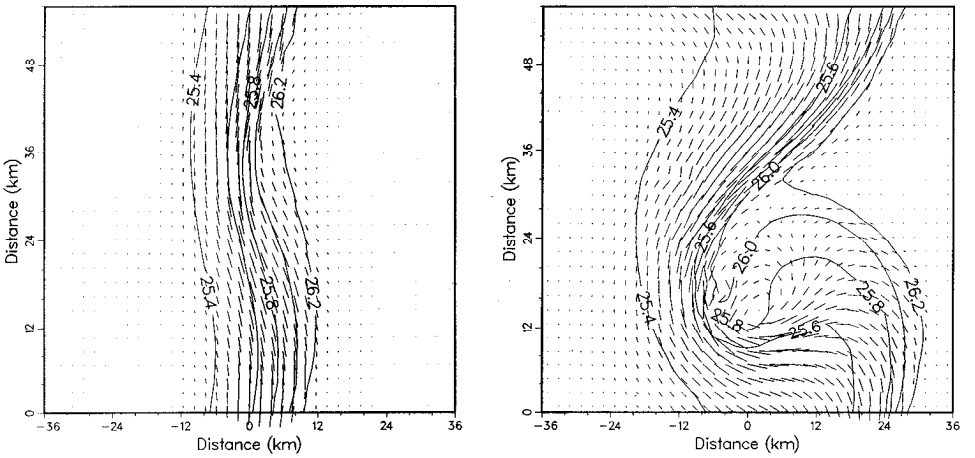

Figure 2. Surface velocity and density distribution for narrow jet: (a) day 1, (b) day 5.

2 km (1 grid interval) and wavelength 60 km. The model was integrated for 9 days. Figure 2 shows surface velocity and density distribution at (a) day 1 and (b) day 5. As the disturbance starts growing (day 1), the along-channel velocities become stronger at wave trough than at wave crest. (The wave trough is defined as the excursion of the jet towards the warm side.) The horizontal velocity shears (relative vorticities) also become larger on the cold (cyclonic) side than on the warm (anticyclonic) side. Both these tendencies continue. On day 5, the cyclonic vorticity becomes so large that the wave crest is bent backward enclosing an isolated eddy. The wave disturbance remains almost stationary; the phase speed is about 5 cm s^{-1}.

Figure 3 shows distributions at day 5 (at $y = 16$ km in Fig. 2b) of (a) density, (b) along-channel velocity, (c) cross-channel velocity, and (d) vertical velocity, in a vertical cross-section intercepting through both wave trough and crest. The density front in the wave trough, σ_t between 25.6 and 26.0, is much narrower ($< L_d$) and steeper than in the initial state (Fig. 3a). The surface jet also becomes narrower, but its maximum velocity remains about the same as in the initial state (Fig. 3b). In contrast, there is no distinct frontal structure in the wave crest. The horizontal circulation is cyclonic in the wave trough and anticyclonic in the wave crest (Fig. 3b). Below 100 m, the flow field is completely dominated by a cyclonic eddy of about 20 km ($2L_d$) wide. The cross-channel velocity is convergent in the wave trough and divergent in the wave crest (Fig. 3c), and the corresponding vertical motion is downward in the wave trough and upward in the wave crest (Fig. 3d). The subduction is concentrated in the frontal zone and is very strong (50–100 m day^{-1}). In contrast, the upwelling is less intense but more widespread.

Figure 4 shows distribution of (a) surface elevation (sea level) and (b) surface absolute vorticity, $f + \partial v/\partial x - \partial u/\partial y$, at day 5. The along-channel velocities general follow closely the elevation contours (Fig. 2b vs Fig. 4a), indicating that the

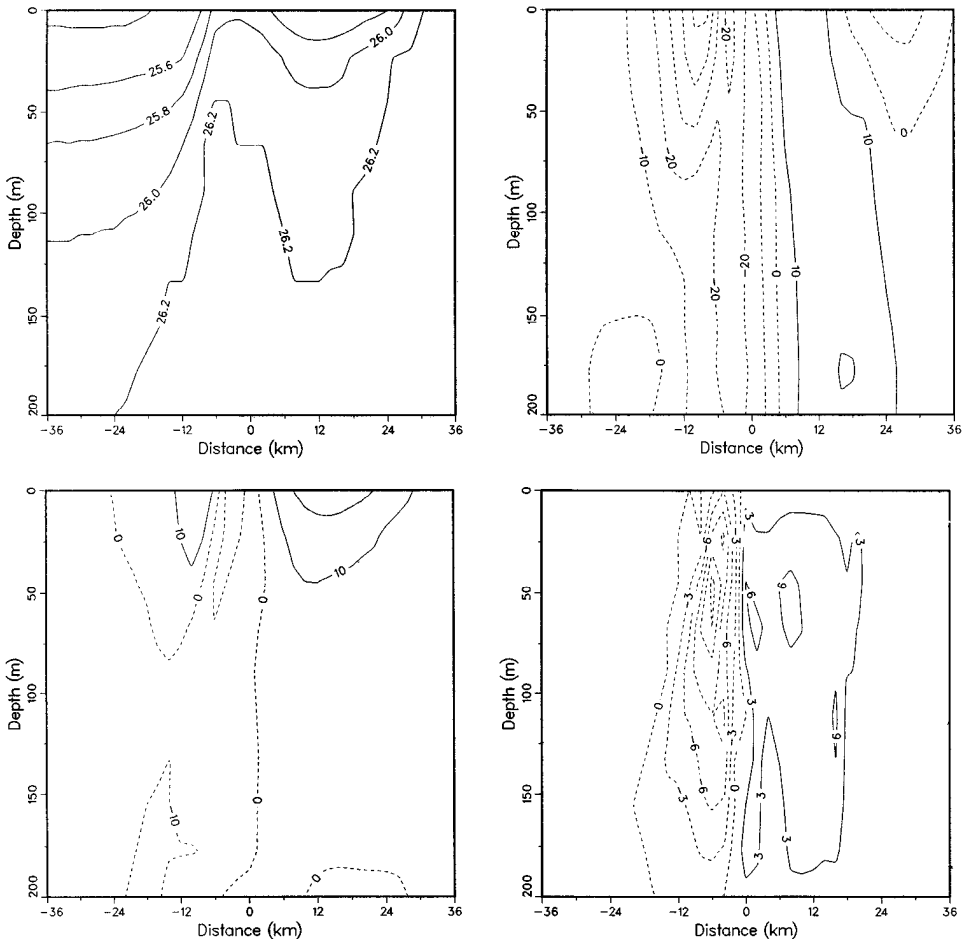

Figure 3. The cross-sectional distribution through the wave trough: (a) density (σ_t), (b) along-channel velocity (cm/s), (c) cross-channel velocity (cm/s) and (d) vertical velocity (10^{-2} cm/s).

along-front velocity is approximately geostrophic. The vorticity distribution, on the other hand, shows a striking asymmetry between cyclonic and anticyclonic vorticity. The cyclonic vorticity is concentrated in a narrow zone along the wave trough, and is exceedingly high (maximum absolute vorticity = $3.5f$). In contrast, the anticyclonic vorticity is widespread and is modest (minimum absolute vorticity = $0.5f$).

Our model results indicate formation of a sharp density front in the wave trough. The frontal zone is marked by strong subduction and high cyclonic vorticity. The mechanism of frontogenesis is best illustrated with semi-geostrophic theory (Hoskins, 1982). The rate of change of the surface horizontal density (temperature)

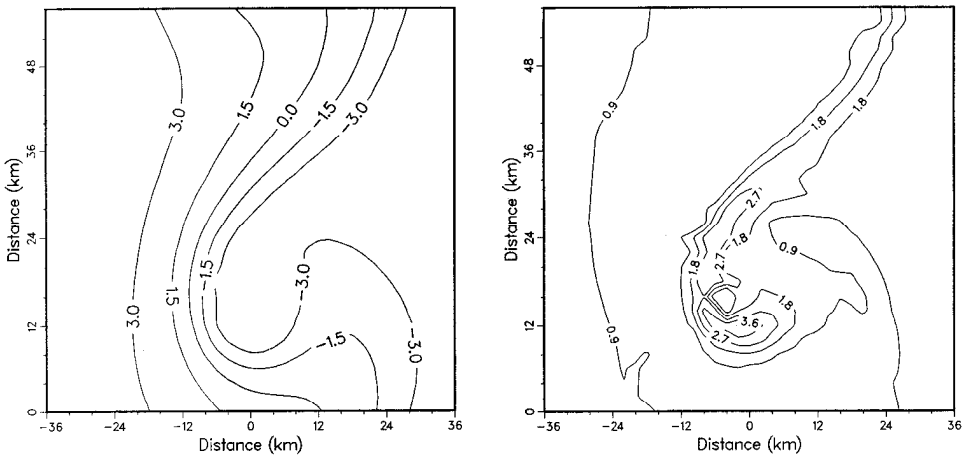

Figure 4. The base case at day 5: (a) surface elevation (cm), and (b) surface absolute vorticity (in unit of f).

gradient following a fluid particle is,

$$\frac{D}{Dt}(|\nabla_x \rho|^2) = -2\alpha_1 \rho_x \rho_y - \alpha_2(\rho_x^2 - \rho_y^2) - \delta |\nabla_x \rho|^2 \tag{7}$$

where ∇_x is the horizontal gradient operator, $\delta = \partial u/\partial x + \partial v/\partial y$, is the horizontal divergence, and $\alpha_1 = \partial v/\partial x + \partial u/\partial y$, $\alpha_2 = \partial u/\partial x - \partial v/\partial y$, are the two components of the deformation field multiplied by 2 (at surface, $w = 0$). Eq. 7 indicates that frontogenesis can be induced by confluence (the first two terms on the RHS) as well as convergence (the last term on the RHS). The synoptic-scale surface flow field is confluent, as indicated by the geostrophic streamlines (constant surface elevations) coming together in the wave trough (Fig. 4a). This would compress density contours, increasing the cross-stream density gradient. In the semi-geostrophic approximation, the downstream velocity is always geostrophic. Thus, an increase in cross-stream density gradient will cause a corresponding increase in geostrophic shear. This can be accomplished by an ageostrophic circulation,

$$\frac{Dv_g}{Dt} + fu_a = 0 \tag{8}$$

where v_g is the geostrophic (downstream) velocity and u_a is the ageostrophic (cross-stream) velocity. The induced surface ageostrophic current is to the left (looking downstream), and it is upward on the warm side and downward on the cold side. The mesoscale ageostrophic convergence in turn will generate an even larger density gradient (Eq. 7). Through feedback, the ageostrophic circulation and horizontal density gradient will continue to increase, resulting in a sharp surface front on the

cold (cyclonic) side. In contrast, the ageostrophic circulation is divergent on the warm side, and no sharp front will develop.

The rate of change of the relative vorticity following a fluid particle is:

$$\frac{D}{Dt}\left(f+\frac{\partial v}{\partial x}-\frac{\partial u}{\partial y}\right)=\left(f+\frac{\partial v}{\partial x}-\frac{\partial u}{\partial y}\right)\frac{\partial w}{\partial z}. \tag{9}$$

In the convergence zone ($\partial w/\partial z > 0$), the increase of positive (cyclonic) vorticity is enhanced by the positive relative vorticity in the RHS of Eq. 9 (the ageostrophic effect). In contrast, in the divergence zone, the increase of negative (anticyclonic) vorticity is restrained due to the counter-balance by the negative relative vorticity in the RHS of Eq. 9. Thus, the cyclonic vorticity eventually must become dominant. The striking asymmetry between cyclonic and anticyclonic vorticities found in our model is evidence of this strong ageostrophic effect. When the Rossby number is $O(1)$, the cyclonic vorticity grows exponentially, and its rate of increase is approximately equal to $w_{z=-h}/h$, where h is the depth of the maximum vertical velocity. For vertical velocity of 50 m day^{-1} and h = 70 m, this yields a growth rate of 1.4 day, which is consistent with the value derived from the energy budget (next section).

b. Energy budget. The unstable wave derives its energy from the basic state. To analyze the energy budget, the total solution is separated into mean and perturbation, where the mean state is defined as the average over wavelength (channel length) and the perturbation is the difference between total and mean (Orlanski and Cox, 1973). For example, $u = \langle u\rangle + u'$, where $\langle u\rangle$ is the mean and u is the perturbation (eddy).

The eddy kinetic energy is:

$$K_e = \langle u'^2 + v'^2\rangle/2;$$

the eddy potential energy is:

$$P_e = g\langle \rho'^2\rangle/(\partial\langle\rho\rangle/\partial z);$$

the energy conversion from mean potential energy to eddy potential energy is:

$$\{P_m P_e\} = -g\langle u'\rho'\rangle(\partial\langle\rho\rangle/\partial x)/(\partial\langle\rho\rangle/\partial z);$$

the energy conversion from mean kinetic energy to eddy kinetic energy is:

$$\{K_m K_e\} = -\langle u'v'\rangle(\partial\langle v\rangle/\partial x) - \langle v'w'\rangle(\partial\langle v\rangle/\partial z);$$

and the energy conversion from eddy potential energy to eddy kinetic energy is:

$$\{P_e K_e\} = -g\langle w'\rho'\rangle.$$

Since in our simulation the initial state changes completely over a few days, the

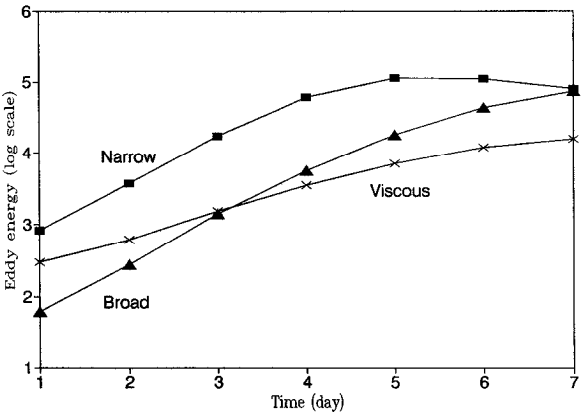

Figure 5. The daily total eddy energy (in natural log scale) for narrow jet (solid square), broad jet (solid triangle) and viscous jet (cross).

choice of a mean state is somewhat ambiguous. (For example, Oey (1988) used the initial state as the mean state.) However, the qualitative nature of the energy budget is clear.

The total energy budget can be conveniently analyzed from the box energy (energy summed over the entire channel width) diagram. Figure 5 shows the daily total eddy energy computed from the base case (marked 'narrow'). The e-folding time (linear growth rate) is about 1.5 day. On day 5 when the total eddy energy is maximum, the major energy transfer terms are: $\{P_mP_e\} = 8.4 \times 10^{-4}$, $\{P_eK_e\} = 5.9 \times 10^{-4}$, $\{K_mK_e\} = -0.4 \times 10^{-4}$ and dissipation $= -4 \times 10^{-4}$. The horizontal heat flux, $\{P_mP_e\}$, is everywhere positive. In other words, the cold water tends to move toward the right (looking downstream) and the warm water toward the left (Fig. 2b). Positive (down-gradient) horizontal heat flux decreases the mean horizontal temperature gradient, converting mean potential energy into eddy potential energy. The vertical heat flux, $\{P_eK_e\}$, also is everywhere positive, that is, the cold water generally moves down and the warm water moves up (Fig. 3d). Positive vertical heat flux decreases the mean vertical temperature gradient, converting eddy potential energy into eddy kinetic energy. This process is characteristic of baroclinic instability.

The horizontal Reynolds stress, $-\langle u'v' \rangle$, is large and is always negative (minimum $= -300$ cm^2 s^{-2}). In other words, the meandering currents tend to deflect gently toward the right (looking downstream), but veer sharply towards the left (Fig. 2b). Despite the large horizontal Reynolds stress, the energy conversion from mean kinetic energy to eddy kinetic energy, $\{K_mK_e\}$, however is small. It is also in the wrong direction (from eddy to mean) for barotropic instability. On day 7 when the wave energy is in an equilibrium (slightly decaying) stage (Fig. 5), the energy transfer terms are: $\{P_mP_e\} = 3.1 \times 10^{-4}$, $\{P_eK_e\} = 3.3 \times 10^{-4}$, $\{K_mK_e\} = -1.0 \times 10^{-4}$ and dissipation $= -3 \times 10^{-4}$. Clearly, the horizontal and vertical heat flux both have

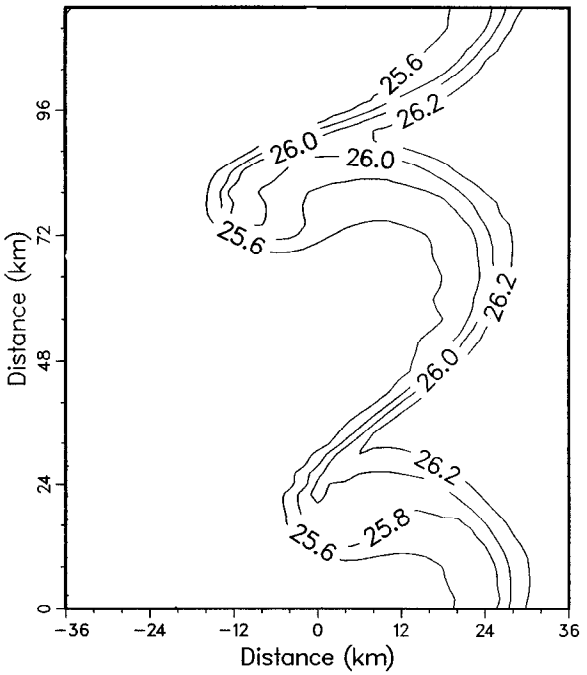

Figure 6. Surface density distribution for narrow jet in a long channel at day 5.

decreased substantially since day 5. In other words, the ageostrophic circulation subsides after the rapid initial growth.

c. Sensitivity analysis. The frontogenesis can be affected by various internal and external model parameters. We examined some factors:

(1) Wavelength

Our choice of wavelength = 60 km follows conventional wisdom. To verify this assumption, the channel length was doubled to 120 km. The initial state contained two equal-amplitude (one grid interval) disturbances with wavelengths of 60 km and 120 km, respectively. Figure 6 shows surface density distribution on day 5. The 60 km wave is completely dominant, which confirms the assumption that the most unstable wave scales as the deformation radius. Figure 6 also conveys the striking asymmetry between wave trough and wave crest.

(2) Ambient flow

The phase speed of frontal waves depends on ambient flow. In the base case, the ambient current is zero outside the initial jet, and the frontal wave is almost stationary (phase speed = 5 cm s^{-1}). The base case was modified to include a uniform 10 cm s^{-1} barotropic flow. Figure 7 shows surface density and velocity distribution on day 5. The amplitude of the frontal wave is little affected by ambient flow, but the wave propagates much faster than in the base case. For example, at day

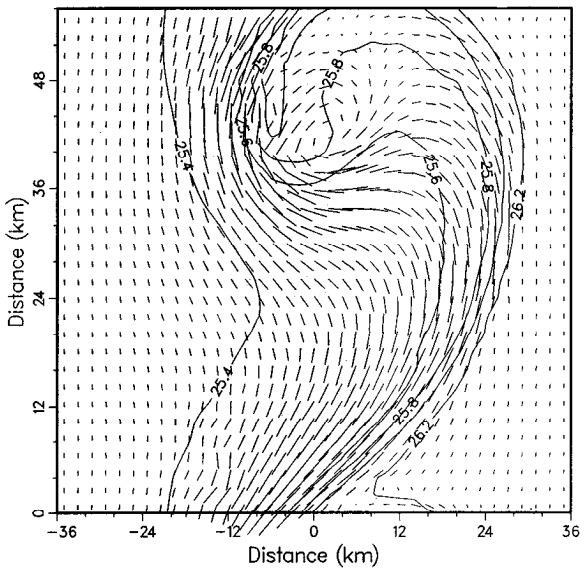

Figure 7. Surface velocity and density distribution for narrow jet with a barotropic flow at day 5.

5 the wave crest has already passed through the open boundary (and reentered from the upstream boundary). The estimated phase speed is about 15 cm s^{-1}, indicating that the frontal wave is mainly advected with the ambient current.

(3) Horizontal eddy viscosity

In the base case, the eddy viscosity A_h is 10^5 cm^2 s^{-1}; the corresponding horizontal Ekman number (which is a measure of the horizontal diffusion), A_h / fL_d^2, is 10^{-3}. The model run was repeated with a larger eddy viscosity, $A_h = 10^6$ cm^2 s^{-1}. Figure 8 shows distributions of (a) surface velocity and density and (b) vertical velocity (at 100 m), on day 5. The baroclinic wave is much weaker than in the base case. The daily eddy energy is included in Fig. 5 (marked 'viscous'). The linear growth rate is only about half of the base case, that is, the e-folding time is about 3 days. The vertical velocity distribution shows subduction at wave trough and upwelling at wave crest. However, the maximum vertical velocity of about 20 m day^{-1} is substantially less than in the base case (Fig. 8b).

(4) Rossby number

In the base case, the mean flow is a narrow jet with $R_o = 0.4$. The initial density distribution tanh $(x/4)$ (Eq. 6) was replaced by tanh $(x/8)$. This yields an initial jet of 40 km wide, a maximum surface current of 25 cm s^{-1}, and a corresponding $R_o < 0.1$. Figure 9 shows surface velocity and density distribution at (a) day 1 and (b) day 5. Even though the wave is not as intense as in the base case (Fig. 2b), a sharp density front, σ_t between 25.6 and 26.0, is formed in the wave trough at day 5. The cyclonic vorticity also is very large (maximum absolute vorticity $> 3f$). The daily total eddy

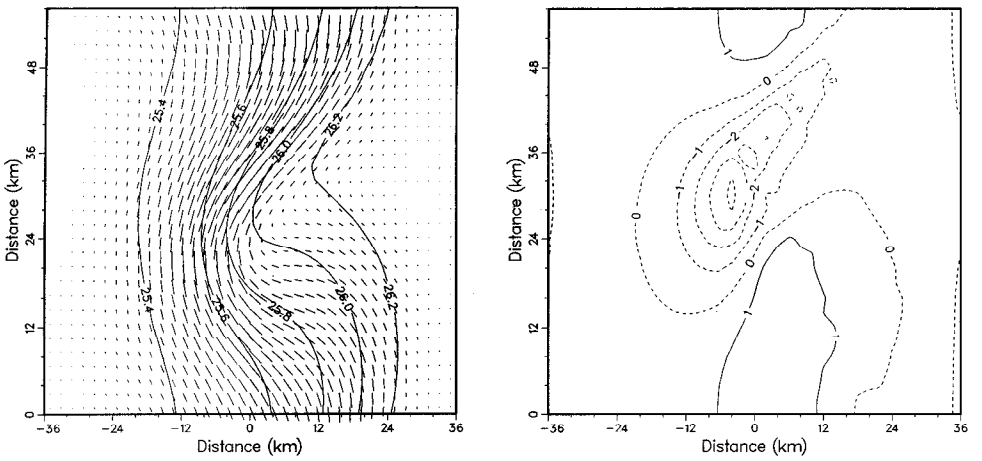

Figure 8. (a) Surface velocity and density distribution and (b) vertical velocity at 100 m (10^{-2} cm/s), for narrow jet with a high eddy viscosity at day 5.

energy is included in Figure 5 (marked 'broad'). The linear growth rate in this case is identical to the base case, suggesting that frontogenesis does not depend on a narrow initial jet.

(5) Ambient stratification

In all test cases, the water column is homogeneous below 100 m (Fig. 1). Since there is no compensating baroclinic pressure gradient in the lower layer, the vertical circulation can penetrate to the bottom (Fig. 3d). To analyze the effects of the main thermocline, we extended the water depth to 300 m, and included a linear stratification (density increases from 26.3 to 26.7 σ_t) between 200 m and 300 m. We repeated the simulation using $A_h = 10^6$ cm^2 s^{-1}. The structure of the baroclinic wave (figure

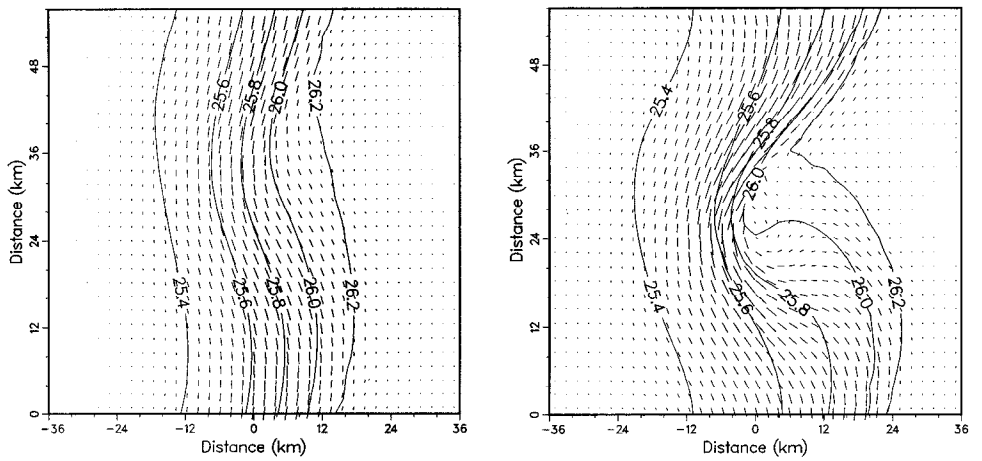

Figure 9. Surface velocity and density distribution for broad jet: (a) day 1, (b) day 5.

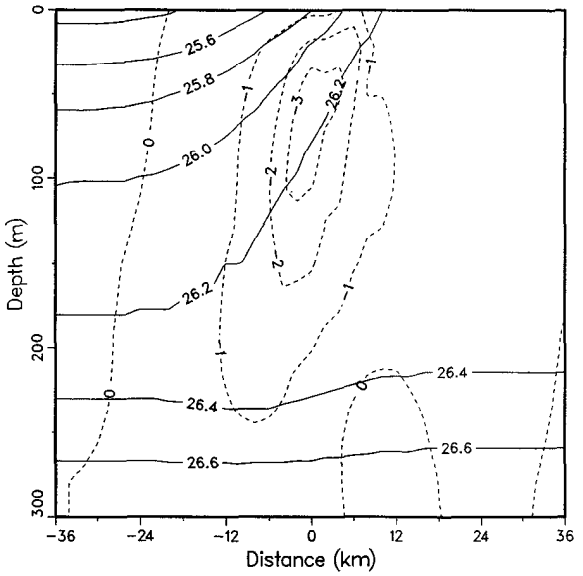

Figure 10. Cross-sectional distribution of density (σ_t) and vertical velocity (10^{-2} cm/s) in a deep channel.

not shown) is similar to the previous run of Figure 8a. Figure 10 shows a density and vertical velocity cross section through the wave trough (at y = 32 km of Fig. 8a) at day 5. The vertical circulation in the upper 200 m is no different from the homogeneous case. However, because of the stratification in the lower water column (the 'thermocline'), the frontal eddy now is confined to the upper water column. This suggests that our model results are equally applicable to the upper-ocean fronts.

4. Comparison with other model results

The linear stability of a baroclinic current can be derived from quasi-geostrophic theory (Pedlosky, 1979). The most unstable wave has wavelength $2\pi L_d$, or 60 km for our model parameters. The growth rate depends on the mean velocity shear. For velocity difference of 30 cm s^{-1} between upper and lower layers (our case; Fig. 1), the e-folding time is 1.5 day. Alternatively, the linear stability of a sloping density interface can be derived from a linear, ageostrophic model (Killworth *et al.*, 1984). For layer thickness of 100 m and density difference of 1 σ_t (our case; Fig. 1), this yields a most unstable wavelength of 60 km and e-folding time of 1.5 day. (In Killworth *et al.*, the mean velocity shear does not enter as an independent parameter.) It is interesting to note that the two linear results are indistinguishable in this application. On the other hand, since the linear stability analysis is valid only for small amplitude, the good agreement between linear growth rate and our calculation (which is for finite amplitude), is probably coincidental. In other words, the sustained

rapid growth found in our calculation should not be interpreted by the linear stability theories.

The stability of the Gulf Stream was examined by Oey (1988) using a nonlinear (primitive-equation) model. He obtained a most unstable wave of wavelength $2\pi L_d$ and growth rate 5 day (model run 2 in his Table 1). His results also showed a clearly defined vertical circulation pattern with subduction at the wave trough and upwelling at the wave crest. The vertical velocity was about 10 m day^{-1}, and was almost symmetrical between upwelling and subduction. Onken (1992) obtained a similar vertical circulation pattern using an isopycnal-coordinate model. Also, the stability of the California Current was examined by Haidvogel *et al.* (1991) using a curvilinear-coordinate model. Their initial condition was more complicated than the monochromatic wave used by Oey (1988). Nevertheless, they found subduction at the wave trough (the northern flank of the emerging filament) and upwelling at the wave crest, and their vertical velocity was also about 10 m day^{-1}.

Compared with our base case, those previous model studies showed much more symmetrical flow patterns and they also had significantly less vertical velocity. This difference can be best understood by examination of the quasi-geostrophic limit of frontogenesis. For $R_o \ll 1$, the three-dimensional time derivative, $D/Dt = \partial/\partial t + u_a\partial/\partial x + v_g\partial/\partial y + w_a\partial/\partial z$, in Eq. 8 is replaced by the time derivative moving with the geostrophic flow, $D_g/Dt = \partial_t + v_g\partial y$. The absolute vorticity $f + \partial v/\partial x - \partial u/\partial y$, on the RHS of Eq. 9 also is replaced by f. By neglecting the ageostrophic advection in the cross-frontal plane of Eq. 8, frontogenesis (sharpening of the initial front) and the associated vertical circulation will be much reduced. Also by neglecting the relative vorticity on the RHS of Eq. 9, the positive and negative vorticity will be more symmetrical. It appears that, despite using primitive-equation models, the previous studies fell within the quasi-geostrophic domain.

Our sensitivity analysis indicated that frontogenesis is curtailed by the larger horizontal eddy viscosity. However, whether this alone can account for the difference between our results and the previous models is not obvious. Numerical smoothing in ocean circulation models is a complex function of model resolution, numerical scheme and eddy coefficients, and it is very difficult to estimate the actual degree of smoothing in a particular model run. For example, even our high viscosity case ($A_h = 10^6$ cm^2 s^{-1}) showed stronger asymmetry and larger vertical velocity than in Oey (1988). This would suggest that the numerical smoothing in Oey (1988) probably was much larger than indicated by his eddy coefficient of 10^4 cm^2 s^{-1}. In the case of Onken (1992) and Haidvogel *et al.* (1991), both solutions might be affected by the use of coordinate transformation which downgrades the second-order accuracy. However, we should caution that since our sensitivity analysis was far from complete, there may be many other factors which affect frontogenesis.

James (1984) also used a primitive-equation model to study the stability of a baroclinic current (the Norwegian Current). The model setting was similar to that of

Oey (1988). However, unlike other earlier studies, he found considerable sharpening of the initial density front after 3 days of simulation. Unfortunately, his model solution was badly contaminated by inertial motion. Since strong convergence was generated by inertial motion at the frontal boundary, it is difficult to sort out the actual case of frontogenesis in his model. James (1984) also did not analyze the distribution of vorticity or vertical velocity.

5. Discussion

Our primitive-equation model results mirrored semi-geostrophic predictions (Hoskins, 1982). The frontogenesis in the wave trough was started by confluence (due to synoptic scale convergence in the baroclinic wave), enhanced by intense surface subduction (due to mesoscale ageostrophic circulation), and was characterized by large cyclonic vorticity and sharpened density gradient. Our model actually went beyond semi-geostrophic theory. We found that the growth of the baroclinic wave was drastically amplified in the case of low viscosity. Since the horizontal Ekman number, $A_h/(fL_d^2)$ was small even for large viscosity, the increased growth rate cannot be attributed totally to the decreased horizontal dissipation. This suggests a feedback mechanism. In other words, the enhanced subduction during frontogenesis also increases the vertical heat flux, which in turn accelerates the baroclinic instability. This feedback mechanism may also explain the explosive ('bomb') nature of mesoscale cyclogenesis. (In mesoscale cyclogenesis, the moisture input is undoubtedly an important factor. However, a large quantity of moist air must first be pumped up by intense uplifting.)

In the coastal ocean, different water masses typically are separated by sharp fronts. To determine the cross-shelf material transport, it is important to understand the rate of exchange, that is, the vertical circulation, across fronts. For a stable shelf-slope front, the mean vertical circulation only can be induced by friction. Earlier two- (Wang, 1984) and three- (Gawarkiewicz and Chapman, 1992) dimensional models of shelf/slope fronts found that the mean vertical velocity was very weak (< 1 m day^{-1}). Such a motion is very small compared to that associated with the frontal waves. This suggests that a significant fraction of the total material transport may take place during intermittent frontal disturbances.

High primary productions, which may be stimulated by the strong vertical circulation, are often found in fronts. Upwelling brings up the subsurface nutrient-rich water while subduction exports the carbon into the ocean interior. Fronts may also provide an important retention mechanism for the transport of larvae. Many pelagic fishes recruit in the nearshore environment, and therefore, the success of recruitment may depend on the interaction between larvae and cross-frontal circulation. Realistic models of biological-physical coupling in coastal and upper ocean will require good understanding of the vertical circulation in frontal zone.

Acknowledgments. This study was supported by the National Science Foundation. The model computing was through the Cornell National Supercomputer Facilities which is sponsored by the National Science Foundation and IBM. I wish to thank Dr. Veronis for his helpful editorial comments.

REFERENCES

Bane, J. M., D. A. Brooks and K. R. Lorenson. 1981. Synoptic observations of the three-dimensional structure and propagation of Gulf Stream meanders along the Carolina continental margin. J. Geophys. Res., *86,* 6411–6425.

Chew, F., J. M. Bane and D. A. Brooks. 1985. On vertical motion, divergence, and the thermal wind balance in cold-dome meanders: a diagnostic study. J. Geophys. Res., *90,* 3173–3184.

Dewey, R. K., J. N. Moum, C. A. Paulson, C. R. Caldwell and S. D. Pierce. 1991. Structure and dynamics of a coastal filament. J. Geophys. Res., *96,* 14885–14908.

Garvine, R. W., K.-C. Wong, G. G. Gawarkiewicz, R. K. Houghton and F. Aikman. 1988. The morphology of shelfbreak eddies. J. Geophys. Res., *93,* 15593–15607.

Gawarkiewicz, G. G. and D. C. Chapman. 1992. The role of stratification in the formation and maintenance of shelf-slope fronts. J. Phys. Oceanogr., *22,* 753–772.

Haidvogel, D. B., A Beckmann and K. S. Hedstrom. 1991. Dynamical simulations of filament formation and evolution in the coastal transition zone. J. Geophys. Res., *96,* 15017–15040.

Hoskins, B. J. 1982. The mathematical theory of frontogenesis. Ann. Rev. Fluid Mech., *14,* 131–151.

James, I. N. 1984. A three-dimensional numerical shelf-sea front model with variable eddy viscosity and diffusivity. Cont. Shelf Res., *3,* 69–98.

Kadko, D. C., L. Washburn and B. Jones. 1991. Evidence of subduction within cold filaments of the north California coastal transition zone. J. Geophys. Res., *96,* 14909–14926.

Kielmann, J. and R. H. Kase. 1987. Numerical modeling of meander and eddy formation in the Azores Current frontal zone. J. Phys. Oceanogr., *17,* 529–541.

Killworth, P. D., N. Paldor and M. E. Stern. 1984. Wave propagation and growth on a surface front in a two-layer geostrophic current. J. Mar. Res., *42,* 761–785.

Lee, T. N. and L. P. Atkinson. 1983. Low frequency current and temperature variability from Gulf Stream frontal eddies and atmospheric forcing along the southeast U.S. outer continental shelf. J. Geophys. Res., *88,* 4541–4567.

Lillibridge, J. L., G. Hitchcock, T. Rossby, E. Lessard, M. Mork and L. Golmen. 1990. Entrainment and mixing of shelf/slope waters in the near-surface Gulf Stream. J. Geophys. Res., *95,* 13065–13087.

Munk, W. and E. R. Anderson. 1948. Notes on a theory of the thermocline. J. Mar. Res., *7,* 276–295.

Oey, L-Y. 1988. A model of Gulf Stream frontal instabilities, meanders and eddies along the continental slope. J. Phys. Oceanogr., *18,* 211–229.

Onken, R. 1992. Mesoscale upwelling and density finestructure in the seasonal thermocline—a dynamical model. J. Phys. Oceanogr., *22,* 1257–1273.

Orlanski, I. and M. D. Cox. 1973. Baroclinic instability in ocean currents. Geophys. Fluid Dyn., *4,* 297–332.

Osgood, K. E., J. M. Bane and W. K. Dewar. 1987. Vertical velocities and dynamical balances in Gulf Stream Meanders. J. Geophys. Res., *92,* 13029–13040.

Pedlosky, J. 1979. Geophysical Fluid Dynamics. Springer-Verlag, 624 pp.

Pollard, R. T. and L. A. Regier. 1992. Vorticity and vertical circulation at an ocean front. J. Phys. Oceanogr., *22,* 609–625.

Rudnick, D. L. and R. A. Weller. 1993. The heat budget in the North Atlantic Subtropical Frontal Zone. J. Geophys. Res., *98,* 6883–6893.

Smolarkiewicz, P. K. 1983. A simple positive definite advection scheme with small implicit diffusion. Mon. Wea. Rev., *11,* 479–486.

Strub, P. T., P. M. Kosro and A. Huyer. 1991. The nature of the cold filaments in the California Current system. J. Geophys. Res., *96,* 14743–14768.

Swenson, M. S., P. P. Niiler, K. H. Brink and M. R. Abbott. 1992. Drifter observations of a cold filament off Point Arena, California, in July 1988. J. Geophys. Res., *97,* 3593–3610.

Wang, D.-P. 1984. Mutual intrusion of a gravity current and density front formation. J. Phys. Oceanogr., *14,* 1191–1199.

—— 1989. Models of mean and tidal flows in the Strait of Gibraltar. Deep Sea Res., *36,* 1535–1548.

Wang, D.-P., M. Vieira, J. Salat, J. Tintore and P. La Vilette. 1988. A shelf/slope frontal filament off the northeast Spanish coast. J. Mar. Res., *46,* 321–332.

Yoder, J. A. 1985. Environmental control of phytoplankton production on the southeastern U.S. continental shelf, *in* Oceanography of the Southeastern U.S. Continental shelf, L. P. Atkinson, D. W. Menzel and K. A. Bush, eds., American Geophys. Union, 93–103.

Received: *2 February, 1993;* revised: *1 June, 1993.*